Aalborg University

DENMARK

Adaptive Damping Control to Enhance Small-Signal Stability of DC Microgrids

Derbas, Abd Alelah; Oshnoei, Arman; Azzouz, Maher; Awad, Ahmed; Blaabjerg, Frede; Anvari-Moghaddam, Amjad

Adaptive Damping Control to Enhance Small-Signal Stability of DC Microgrids

Abd Alelah Derbas, Arman Oshnoei, *Member, IEEE*, Maher Azzouz, *Senior Member, IEEE*, Ahmed S. A. Awad, *Senior Member, IEEE*, Frede Blaabjerg, *Fellow Member, IEEE*, and Amjad Anvari-Moghaddam, *Senior Member, IEEE*

Abstract—This paper proposes an adaptive active control approach for damping the low-frequency oscillations in a DC microgrid (DC-MG). The DC-MG is comprised of hybrid power sources (HPSs) formed by a parallel set of supercapacitor modules and photovoltaic systems. The HPS controller includes a multi-loop voltage controller for adjusting the DC-MG voltage and a virtual impedance loop for damping current oscillations. The virtual impedance loop is augmented to the inner loop of the voltage controller. An adaptive tuning strategy is developed to adjust the damping coefficient of the virtual impedance loop optimally. In the tuning process, small-signal analysis is used to determine an initial adjustment for the damping coefficient. Subsequently, an approach based on intelligent neural network is intended to provide accurate online correction of the damping coefficient, which passes the dependency of the converter control system on the operating point conditions and accommodates different operation conditions. A sensitivity analysis is also conducted to investigate the effects of the system parameters on the HPS stability. Moreover, a mesh analysis is carried out to examine the stability of low-frequency modes of the whole DC-MG using the proposed control scheme. Case studies are conducted to demonstrate the performance of the proposed control strategy, and the analysis results are verified by Hardware-in-the-Loop (HIL) setup using OPAL-RT (OP5600) and dSPACE (DS1202) simulators.

Index Terms—Intelligent neural network, DC microgrid, virtual impedance loop, stability analysis.

I. INTRODUCTION

DC-microgrids (DC-MGs) have recived great attention in the last decade due to the increasing growth of clean and sustainable energy resources such as photovoltaic (PV) systems, fuel cell (FC), and supercapacitor (SC) modules as storage. These energy systems have a comprehensive integration with DC loads. The topology of a DC-MG in which distributed generators (DGs) along with AC grid, and loads are connected to the common DC line through power electronics converters [1]-[3]. To fully satisfy load requirements and accurately support

Abd Alelah Derbas is with the Department of Energy, Aalborg University, 9220 Aalborg, Denmark, and also with the Faculty of Electrical Engineering, Shahid Beheshti University, Tehran, Iran, (email: aade@energy.aau.dk; a_derbas@sbu.ac.ir).

Arman Oshnoei, Frede Blaabjerg, and Amjad Anvari-Moghaddam are with the Department of Energy, Aalborg University, 9220 Aalborg, Denmark, (email: aros@energy.aau.dk; fbl@energy.aau.dk; aam@energy.aau.dk).

A. S. A. Awad is with the Department of Electrical and Computer Engineering, University of Windsor, Windsor, ON N9B 3P4, Canada, and also with the Electrical Power and Machines Department, Faculty of Engineering, Ain Shams University, Cairo 11566, Egypt (email: a.samir@eng.asu.edu.eg).

Maher Azzouz is with the Department of Electrical and Computer Engineering, University of Windsor, Windsor, ON N9B 3P4, Canada, and is currently on leave with the Electrical Engineering Department, Qatar University, Qatar (email: mazzouz@uwindsor.ca).

transients, the DGs comprise hybrid power sources (HPSs). The HPS offers superior reliability and power quality.

In addition, various advantages of utilizing DC-MG include high power quality, low power losses with high efficient energy conversion, and no synchronization issues [4], [5]. In contrast, there are some technical challenges when designing such energy systems, including effective energy management for organizing the power-sharing with different DGs, regulating the DC bus voltage, meeting the power demand, and ensuring the system stability. Time-scale hierarchically controls, therefore, are required to control DC-MGs and deal with the aforementioned challenges [6]-[8].

Most attention has been focused on the stability problem in DC-MGs, where stability concerns are exhibited by interactions between converters, control units, grid, and loads. When power electronic converters are tightly controlled, they act as constant power loads (CPLs). The stability problem is associated with the negative incremental impedance characteristics in CPLs, which may cause instability in the DC bus, and thus the entire MG may fail [9], [10]. The reason behind this instability is sufficiently described in the previous studies using small-signal impedance-based analyses [11], eigenvalue analyses [12], and passivity-based analyses [13]. To mitigate the instability problem caused by the CPLs, several stabilizing strategies have been presented. From a physical viewpoint, the strategies can be divided into passive and active damping methods. The passive damping method includes a required resistor or capacitor [14] or LC filters [15]. Nevertheless, these strategies demand extra costs and physical restrictions [16]. Introducing virtual impedance loops to converter control systems offer promising solutions for increasing the precision of power-sharing and damping oscillatory currents in MGs [3], [17]-[21]. In [3], a virtual negative inductor stabilizer is formed on the source-side converter to enhance the DC-MG stability. A virtual positive-damping modified impedance is proposed in [17] to improve the stability margin and decrease the voltage drop in DC bus voltage. A feedforward control loop is developed in [18] to address the active damping problem for a buck converter interfaced with CPL. In that design, a low-pass filter's cutoff frequency needs to be adjusted. In [19], a virtual impedance control method is proposed to withdraw the negative incremental impedance characteristic of the CPL, thereby enhancing the DC system stability. In [20], a negative virtual impedance is incorporated into the droop control loop to offset the effect of line inductance and CPL changes. In addition, a control approach based on modifying the output impedance of converters is investigated in [21] to improve the transient response in DC-MGs. This control approach includes

a virtual capacitance and a virtual inductance. Although these methods enhance the stability margin of DC-MGs, they are only applicable to single-bus DC-MGs.

The interaction dynamics of the whole DC-MG can be affected by various factors, including voltage and current controllers' parameters, load types, and line parameters. This interaction can lead to high-frequency power oscillations [22], [23]. With this regard, virtual-impedance loops have been introduced in [22] and [23] to dampen high-frequency oscillations efficiently. Another critical challenge of DC-MGs is low-frequency oscillation arising from power/current-sharing strategies in droop-controlled DC-MGs [24]-[26], which increase with CPLs and electric springs [27]. In [24]-[26], virtual-impedance-based strategies, realized by feed-forward or feedback of disturbance variables, are proposed to alleviate the low-frequency problem made by the droop controllers of DC-MGs. In [28], a virtual series RC-based active damping control strategy is presented for DC/DC converters loaded by CPLs to improve their dynamic response and give stabilization within the DC-MG. The performance of virtual impedance-based methods is deeply influenced by the systematic gains, the tuning of which is still a challenge to be undertaken. The active damping approaches proposed in the previous studies were designed based on a small signal model. Although various linear control techniques can be easily applied into the small-signal model for analysis or control, the stability around the operating point can be ensured. However, providing a uniform and satisfactory control performance over the entire operating range is not easy. If a significant disturbance occurs, these linear control methods may become inefficient, and the system may become unstable because of the CPL. A comprehensive comparison of state-of-the-art strategies used to improve the stability of DC-MGs is summarized in Table I.

Motivated by the previous discussions, this paper presents a novel active damping scheme for HPSs used in DC-MGs. The proposed approach uses a virtual resistive impedance loop to efficiently eliminate the low-frequency current oscillations. It relies on feedforwarding the DG output and is introduced to the inner loop of the voltage controller. A tuning method is embedded in the HPS control structure. In the tuning process, the small-signal analysis provides proper initial adjustment for the damping coefficient of the virtual impedance loop. Then, to avoid the dependency of the response of the converter control system on the operating conditions, the damping coefficient is modified online using an intelligent neural network (INN) method. An eigenvalue analysis is performed to study the impact of the control system parameters on the stability of the low-frequency modes of the DGs. Mesh analysis is also used to obtain the frequency and damping factor of oscillations in the entire DC-MG. A Hardware-in-the-Loop (HIL) setup is implemented using OPAL-RT and dSPACE simulators to validate the proposed control scheme and its success.

II. PROPOSED CONTROL SYSTEM

A. Multi-bus DC-MG Configuration

The single-line diagram of a multi-bus DC-MG with a nominal voltage of 48 V is depicted in Fig. 1. DC-MG connects to the main ac grid through a dc/ac interlink converter; it
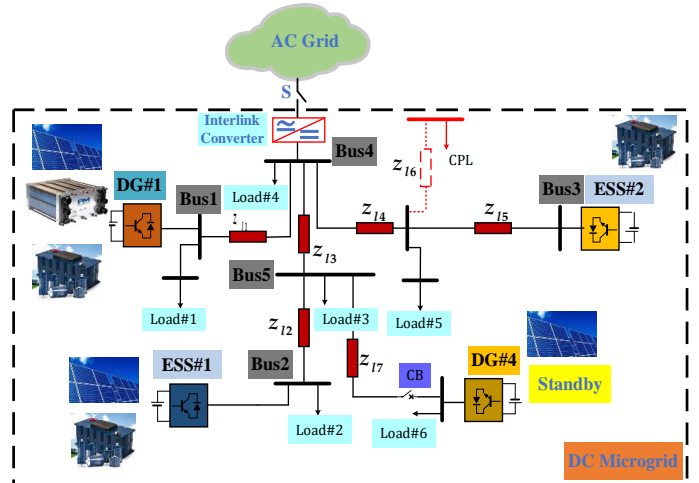

Fig. 1: Single-line diagram of a multi-bus DC-MG

consists of two DG units, two Energy Storage Systems (ESSs), four local, and remote loads. The DG units are connected through impedance lines and operate in voltage control mode. The DC-MG is assumed to operate in an islanding mode. Table I summarizes the parameters of the studied DC-MG including DGs, line impedances, and loads.

DG1 unit comprises an HPS that integrates SC and PV systems. ESS1 and ESS2 incorporate an SC system. DG4 includes a PV system working in standby mode. The HPS supplies steady-state power demand, outstanding power quality, and fast dynamic response. Fig. 2 shows the proposed HPS structure and its schematic of closed-loop control. The SC unit is connected to the dc-link through a bidirectional dc-dc buck converter and it is responsible for regulating the dc-link voltage. In addition, the SC serves as an energy storage source (ESS) to provide the demand loads. At the same time, the PV unit is connected to the dc-link through a unidirectional dc-dc buck converter, which is controlled to reach MPPT and does not need to establish the voltage of the source bus. The parameters of the buck converter used for PV and SC, including inductance, resistance, capacitance, and frequency switching, are equal to 4.5 mH, 0.02 Ω, 75 μF, 20 kHz, respectively.

B. Control Units & Tuning of Parameters

A comprehensive control strategy is proposed for the DG unit-based HPS to enhance the dynamic characteristics and increase the current sharing accuracy. Moreover, to fully satisfy the load demands and sustain a constant DC bus voltage, the HPS system control is provided with two controllers for the PV and SC converters. The PV array controller is adopted to track MPPT swiftly, where the input parameters of the PV converter, the input voltage $V_{C_{pv}}$ and the input current I'_{pv} are measured frequently. The MPPT algorithm utilizes these parameters to calculate the reference power that the PV panel requires to operate at MPPT conditions and to track the PV arrays' maximum power point swiftly. The signal from the MPPT controller is compared with the measured value $V_{C_{pv}}$ and then regulated using a PI controller to generate the PWM signal. The PI controller parameters are chosen as $K_{P_{pv}} = 0.01$

TABLE I: Features of different studies in the stability of DC-MG

Method Description	Advantages	Disadvantages
Virtual impedance to cancel out LF oscillation caused by droop control [24]-[25]	• Improving LF power oscillations damping • Exhibiting suitable transient responses for various load	• Weak performance for dynamic source changes • Poor robustness against unknown line impedance • Low current-sharing accuracy
Virtual impedance to eliminate HF oscillation [22]-[23]	• Active for HF power oscillations • Exhibiting suitable transient responses for various load	• Limited bandwidth • Poor damping for LF oscillations • Poor robustness against unknown line impedance
Virtual impedance to cancel out the negative impedance characteristics of CPLs [3],[18],[20]-[21]	• Enhancing the system damping • Good dynamic response	• Closed-loop bandwidth limitation • Poor to damp LF oscillations • Poor robustness against the dc cable variations
Virtual-positive reshaped-impedance to correct negative resistance characteristic of CPLs [17],[19]	• Improving the LF oscillations • Robustness against the dc cable variations	• Low current-sharing accuracy • Complex implementation
Using hybrid control based on ACS and droop controls [26]	• Active for LF oscillations • Satisfactory performance for various disturbance scenarios	• Need to low-bandwidth communication • High cost

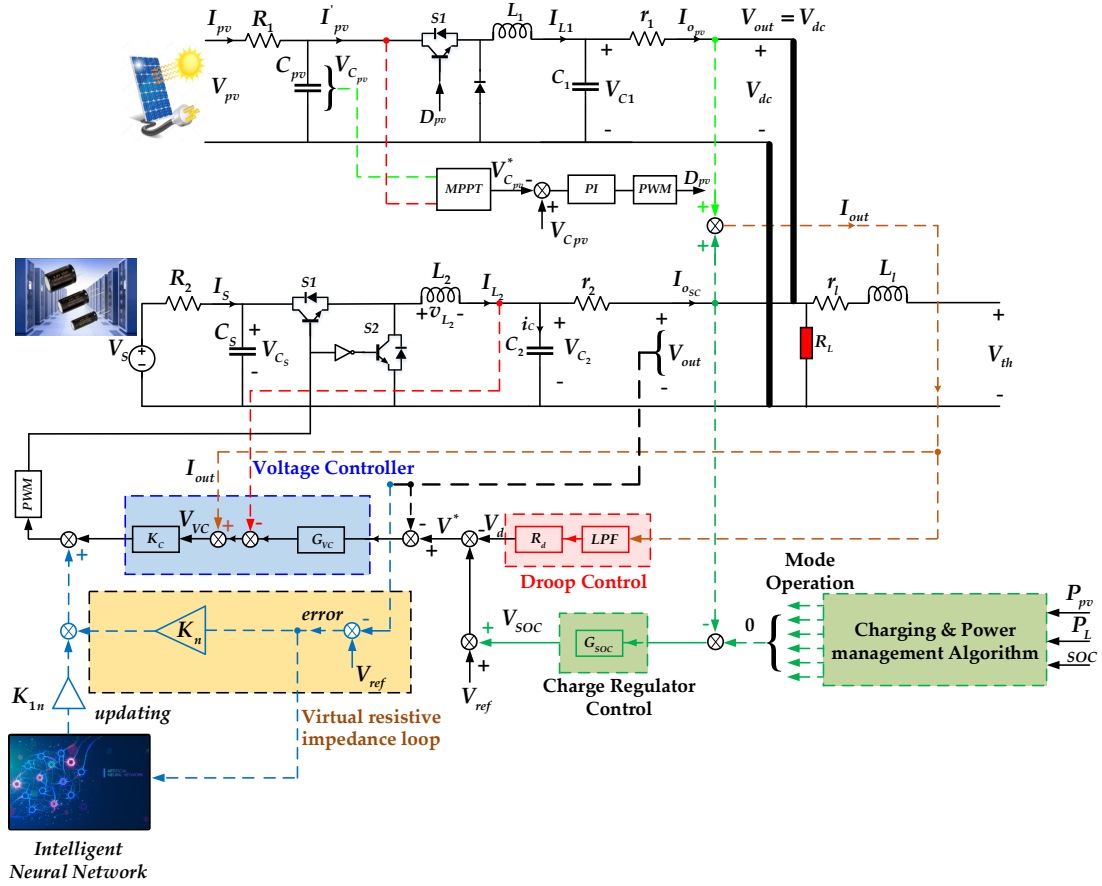LF: Low-Frequency   HF: High-Frequency

Fig. 2: The block-diagram of the proposed control of the DG unit-based HPS
.

and $K_{I_{pv}} = 0.05$. The SC module offers efficient performance, convenient operation for essential sources, and guarantees the system's power quality; therefore, SC is deemed as a fast response power supply integrated with a high-performance dynamic control system. The proposed closed-loop control of the SC converter consists of an inner loop and an outer loop.
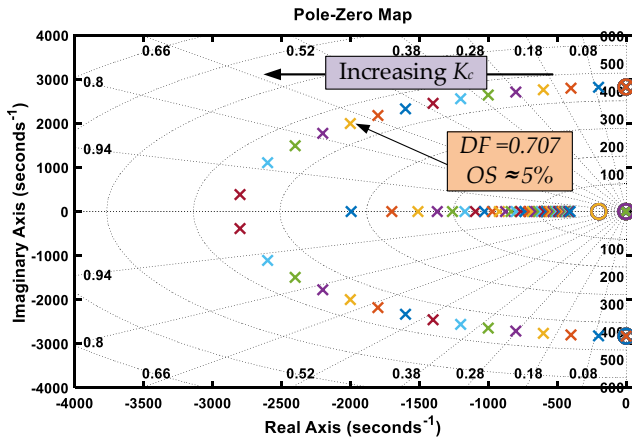
Fig. 3: Dominant poles of open loop control when $K_c(s)$ varies from 1 to 50.

Fig. 4: Frequency response of the open-loop control system of converter without/with $G_{vc}(s)$.

Here, the inner loop is a current controller which performs three main tasks: 1) increased internal stability of voltage closed-loop control, 2) preserving the switches of SC converter upon any over-current, and 3) excluded the influence of the dynamic load variations. Furthermore, the inner loop is composed of two cascaded control loops, including a proportional controller (K_c) to decrease the output impedance and a feed-forward controller to decrease the reaction of load dynamics. The feed-forward controller is provided with the difference between the inductance current and the output current of the converter. Based on the open-loop control system, the variation of eigenvalues can be obtained, as shown in Fig. 3. It can be seen from that figure that all the eigenvalues will go more to the left half-plane with the increasing proportional gain K_c. This shows that the system becomes more stable as K_c increases. The K_c gain is precisely determined based on the standard values of damping ratio and overshoot of the dominant poles of the current loop, which are chosen as 0.7 and 5%, respectively. The K_c gain is obtained equal to 10. The voltage control loop includes a PI controller ($G_{vc}(s)$). By analyzing the frequency response of the open-loop control system, the PI parameters k_{pv} and k_{iv} are set equal to 2 and 150, respectively. These values are obtained in proportion to a phase margin of 58° and a bandwidth of 2 kHz. Fig. 4 shows the frequency response of the open-loop control system of the converter.

As the DC-MG comprises DGs with different energy capacities, the voltage closed-loop control is integrated with the current sharing control unit. Therefore, a droop control loop is designed. The notation R_d in Fig. 2 denotes the droop coefficient, which is determined based on the maximum allowable voltage drop value at the rated current.

The optimal operation of the SC module is proportional to the load requirements in the transient conditions for estimating the state of charge (SOC). An energy management strategy between the SC and PV systems is proposed to obtain the most efficiency from the SC module and preserve the SC module's lifetime. The proposed strategy is shown in Fig. 5. The essential factor for this strategy is the power level supplied by the PV system and the SOC of the SC module. The management strategy allows the highest power from the PV system and
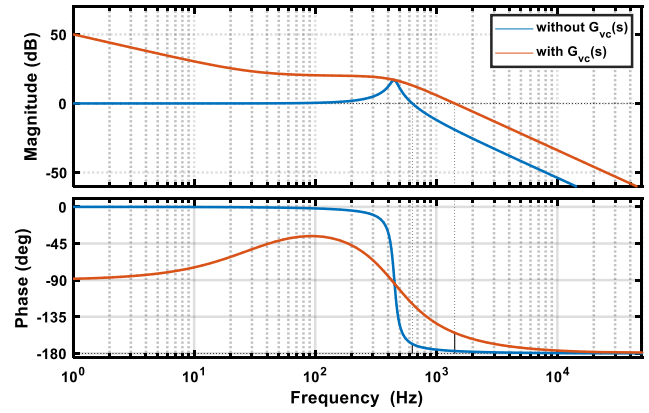
protects the SC modules against depth discharge and overcharge while meeting the energy requirements. It is supposed that the SC modules are charged initially. The management control mainly deals with the load's power supply and the batteries' safety (a minimum and maximum of SOC are considered). The different modes for the system's operation are as follows (Fig. 5)

- **Mode 1:** The PV power is sufficient to supply the load, and SC is in charging mode.
- **Mode 2:** The PV power is sufficient to supply the load, and SC is completely charged.
- **Mode 3:** The SC supplies the load when there is no power from the PV system.
- **Mode 4:** The PV power is insufficient to supply the load, and the SC is discharged.
- **Mode 5:** There is no power from the PV (during cloudy day or night), and SC is completely discharged; thus, the load will be disconnected.

An SOC regulation control loop is also introduced to the closed-loop system to enhance the dynamic performance. A PI controller is adopted for this purpose. The PI parameters are tuned such that a fast response is achieved to supply the required energy with no effect on the dynamic performance of DC-MG is achieved. The controllers' parameters are given in Table II. As Fig. 2 illustrates, an adaptive virtual resistive impedance loop is used as a feed-forward of the output voltage error to improve the dynamic performance of the SC control system. An INN-based method determines the gain associated with the virtual resistive impedance loop. The design process of the INN-based regulation scheme will be discussed in Section V.

III. MODELING

1) Supercapacitor System: The SC is the main energy storage source, and it effectively reduces the grid oscillations due to its fast response, which will also lead to good power quality. A bidirectional-buck converter connects the SC to the DC link, whose parameters of inductance, resistance, capacitance, and frequency switching are equal to 4.5 mH, 0.02 Ω, 75 μF,
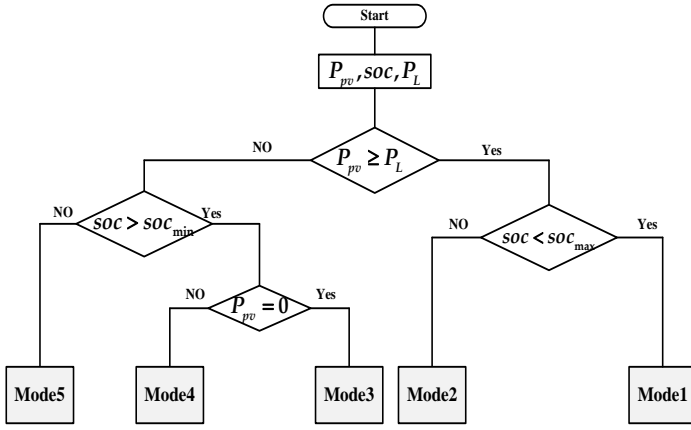
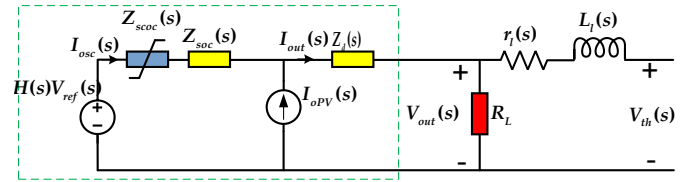Fig. 5: Energy management strategy between SC and PV systems

Fig. 6: Equivalent small signal model of HPS.

to provide suitable damping far away from the switching ripple-frequencies over 20 kHz. $v_{soc}(s)$ is obtained as follows:

$$v_{soc}(s) = -I_{o_{sc}}(s)G_{soc}(s) \tag{8}$$

Substituting (7) and (8) in (6) and then in (4) yields

$$V_{out}(s) = H(s)V_{ref}(s) - (z_{sc_{oc}}(s) + z_{soc}(s))I_{o_{sc}}(s) - z_d(s)I_{out}(s) \tag{9}$$

where $I_{out}(s)$ is the output current of the hybrid system, which is expressed as

$$i_{out}(s) = I_{o_{sc}}(s) + I_{o_{pv}}(s) \tag{10}$$

where

$$z_d(s) = \frac{\omega_{fd}}{s + \omega_{fd}} R_d H(s) \tag{11}$$

$$z_{soc}(s) = \left(k_p + \frac{k_I}{s}\right) H(s). \tag{12}$$

20 kHz respectively. The average state-space model of the SC converter is given as follows:

$$\dot{V}_{C_s} = \frac{1}{R_2 C_s} V_s - \frac{1}{R_2 C_s} V_{C_s} - \frac{1}{C_s} I_{L_2} u_2 \tag{1}$$

$$\dot{V}_{C_2} = \frac{1}{r_1 C_2} V_{dc} - \frac{1}{r_1 C_2} V_{C_2} + \frac{1}{C_2} I_{L_2} \tag{2}$$

$$\dot{I}_{L_2} = -\frac{1}{L_2} V_{C_2} + \frac{1}{L_2} V_{C_s} u_1 \tag{3}$$

where V_s is the supercapacitor's voltage; V_{C_s} and V_{C_2} are the voltages of capacitors C_s and C_2, respectively; I_{L2} is the current of inductor L_2. R_2 and r_2 are the resistances representing the cable losses, and u_2 is the duty cycle of the SC converter.

2) Closed-Loop Control of SC Converter: The output voltage of the SC converter can be written based on the reference voltage $V^*(s)$ and the output current $I_{o_{sc}}(s)$ as follows:

$$V_{out}(s) = H(s)V^*(s) - z_{sc_{oc}}(s)I_{o_{sc}}(s) \tag{4}$$

where $z_{sc_{oc}}$ denotes the closed loop output impedance of the SC converter; and $H(s)$ is a transfer function that is calculated by dividing $V_{out}(s)$ by $V^*(s)$, as given by

$$H(s) = \frac{V_{out}(s)}{V^*(s)}\Big|_{I_{osc}=0} \quad z_{sc_{oc}}(s) = -\frac{V_{out}(s)}{I_{o_{sc}}(s)}\Big|_{V^*(s)=0}. \tag{5}$$

The reference control signal $V^*(s)$ is generated based on the subtraction of the SOC regulation control output ($V_{soc}(s)$) and droop control output ($V_d(s)$), represented by

$$V^*(s) = V_{ref}(s) + V_{soc}(s) - V_d(s) \tag{6}$$

where $V_{ref}(s)$ is the nominal voltage of the DC-MG. The V-I characteristic of the droop control loop is obtained from Fig. 2 as follows:

$$v_d(s) = \frac{\omega_{fd}}{s + \omega_{fd}} R_d I_{out}(s) \tag{7}$$

where ω_{fd} denotes the cut-off frequency of the low-pass filter included in the droop unit. ω_{fd} is chosen equal to 10π rad/sec

TABLE II: Parameters of DC-MG

Symbols	Description	Value
r_l (mΩ)	Line parameters	3.46, 3.46, 6.91, 3.46, 6.91, 6.91
l_l(μH)		2.2, 2.2, 4.4, 2.2, 4.4, 4.4
P_l (kW)	Power of load	0.5, 0.5, 0.7, 1.5, 1
P_{DG_i} (kW)	Power of DG	1+5, 2.5, 1.25, 1
	Type source	PV+SC, SC, SC, PV (S.b.)∗
V_{ref} (V)	DC-MG voltage	48
V_{pv} (V)	PV voltage	70-150
C_j (μF)	Capacitor of converter	75
L_j (mH), r_j (Ω)	Inductance of converter	4.5, 0.02
f_{SW} (kHz)	Switching frequency	20
$l = 1, .., 6,$	$i = 1, .., 4,$	$j = 1, 2$ ∗S.b. = Standby

TABLE III: Controllers' parameters

Controller	K_p	K_I	
Voltage controller	3	250	
Charging controller	0.02	0.07	
PI controller of PV	0.01	0.05	
Current controller	15	−	
Droop coefficient	R_{d1}	R_{d2}	R_{d3}
	0.057	0.114	0.228

The equivalent model of the closed-loop control is illustrated in Fig. 6. As presented, the HPS system is modeled by an independent voltage source in series with variable impedance, which depicts the closed-loop impedance of the SC converter. The PV system is modeled by a parallel independent current source with low dynamic response characteristics.

By using the Thevenin's equivalent for the rest part of the DC-MG, the output current of the HPS can be calculated as follows:

$$V_{out}(s) - V_{th}(s) = \left(I_{out}(s) - \frac{V_{out}(s)}{R_L}\right) Z_l(s) \quad (13)$$

Substituting $I_{o_{sc}}(s)$ from (10) in (9) and then substituting $V_{out}(s)$ in (13) leads to (14)

Then, the characteristic equation of the closed-loop system can be obtained as follows:

$$z_{out}(s)\left(R_L + z_l(s)\right) + R_L z_l(s) = 0 \quad (15)$$

where

$$z_l(s) = r_l(s) + sL_l(s) \quad (16)$$

where $z_{out}(s)$ denotes the output impedance of the HPS system, which is expressed as follows:

$$z_{out}(s) = z_{sc_{oc}}(s) + z_{soc}(s) + z_d(s) \quad (17)$$

Substituting (14) and (15) in (18) yields (21) as follows:

$$(z_{sc_{oc}}(s)+(k_p + \frac{k_i}{s})H(s) + \frac{\omega_{fd}}{s+\omega_{fd}}R_d H(s))\times \quad (18)$$
$$(R_L + (r_l + sL_l)) + R_L(r_l + sL_l) = 0.$$

As (21) implies, the roots of the characteristics equation are influenced by the DG system parameters. A sensitivity analysis is addressed in the next section to investigate the effects of the system parameters on the DG stability.

3) Small-Signal Model of HPS System Considering the PV Converter Dynamics: The PV is an auxiliary source in the DC-MG, and it is estimated according to the MG's load. A unidirectional-buck converter connects the PV to the DC bus. The average state-space model of the PV converter is expressed as follows:

$$\begin{cases} \dot{i_{L1}} = -\dfrac{r_{l1}}{L_1}I_{L1} - \dfrac{1}{L_1}v_{C1} + \dfrac{1}{L_1}v_{C_{pv}}d_{pv} \\ \dot{v_{C1}} = \dfrac{1}{C_1}i_{L1} - \dfrac{1}{C_1}i_{o_{pv}} \end{cases} \quad (19)$$

$$v_{out} = \begin{bmatrix} 0 & 1 \end{bmatrix} \cdot \begin{bmatrix} i_{L1} \\ v_{C1} \end{bmatrix} + r_1 \cdot i_{o_{pv}} \quad (20)$$

where $v_{C_{pv}}$ and v_{C_1} represent the voltages of capacitors C_{pv} and C_1, respectively; i_{L_1} and $i_{o_{pv}}$ are the current of inductance L_1 and output current, respectively; r_{l1} is the inductor resistance; r_1 is a resistance representing the cable losses; and d_{pv} denotes the duty cycle for on-state of the switch.

The variables in (19) and (20) can be written as the sum of the steady-state value and the disturbance $(x = \bar{\mathbf{X}} + X)$, then the small-signal model can be obtained as:

$$\begin{bmatrix} \dot{I_{L1}} \\ \dot{V_{C1}} \end{bmatrix} = A_1 \cdot \begin{bmatrix} I_{L1} \\ V_{C1} \end{bmatrix} + A_2 \cdot I_{o_{pv}} + A_3 \cdot V_{C_{pv}}$$
$$+ A_4 \cdot D_{pv} \quad (21)$$

$$V_{out} = B_1 \cdot \begin{bmatrix} I_{L1} \\ V_{C1} \end{bmatrix} + B_2 \cdot I_{o_{pv}} \quad (22)$$

in which

$$A_1 = \begin{bmatrix} -\dfrac{r_{l1}}{L_1} & -\dfrac{1}{L_1} \\ \dfrac{1}{C_1} & 0 \end{bmatrix} \quad A_2 = \begin{bmatrix} \dfrac{\bar{V_{C_{pv}}}}{L_1} \\ 0 \end{bmatrix}$$

$$A_3 = \begin{bmatrix} 0 \\ -\dfrac{1}{C_1} \end{bmatrix} \quad A_4 = \begin{bmatrix} \dfrac{\bar{D_{pv}}}{L_1} \\ 0 \end{bmatrix} \quad (23)$$

$$B_1 = \begin{bmatrix} 0 & 1 \end{bmatrix} \quad B_2 = -r_1 \quad (24)$$

By transferring the linear small-signal model in (21) and (22) into the frequency domain, the output voltage is obtained as follows

$$V_{out}(s) = \left[B_1\left(sI - A_1\right)^{-1}A_2\right] \cdot D_{pv}(s)$$
$$+ B_1\left(sI - A_1\right)^{-1}A_4 \cdot V_{C_{pv}}(s)$$
$$- \left[-B_1\left(sI - A_1\right)^{-1}A_3 - B_2\right] \cdot I_{o_{pv}}(s). \quad (25)$$

From Fig. 7, D_{pv} is is given as

$$D_{pv} = \left(V_{C_{pv}}^*(s) - V_{C_{pv}}(s)\right) \times G_{pi_{pv}}(s)G_{pwm}(s) \quad (26)$$

where $G_{pwm}(s)$ is the transfer function of PMW generator and $G_{pi_{pv}}(s)$ is the PI controller used to regulate the output voltage $V_{C_{pv}}^*$. Here, the impact of MPPT on PV is represented by the perturbation in the reference value of the PV output voltage $V_{C_{pv}}^*$.

$$V_{out}(s) = \left[B_1(sI - A_1)^{-1}A_2\right] \cdot G_{pi_{pv}}G_{pwm} \cdot V_{C_{pv}}^*(s)$$
$$+ \left\{B_1(sI - A_1)^{-1}A_4 - \left[B_1(sI - A_1)^{-1}A_2\right]\right.$$
$$\left. \times G_{pi_{pv}}G_{pwm}\right\} \cdot V_{C_{pv}}(s)$$
$$- \left[-B_1(sI - A_1)^{-1}A_3 - B_2\right] \cdot I_{o_{pv}}(s). \quad (27)$$

where

$$G_{11}(s) = \left(B_1(sI - A_1)^{-1}A_2\right) \times G_{pi_{pv}}G_{pwm}$$
$$G_{21}(s) = \left(B_1\left(sI - A_1\right)^{-1}A_4\right) - \left(D_1\left(sI - A_1\right)^{-1}A_2\right.$$
$$\left. \times G_{pi_{pv}}G_{pwm}\right)$$
$$z_{o_{pv}}(s) = -B_1\left(sI - A_1\right)^{-1}A_3 - B_2. \quad (28)$$

Then (27) can be written as:

$$V_{out}(s) = \left[G_{11}(s) \cdot V_{C_{pv}}^*(s) + G_{21}(s) \cdot V_{C_{pv}}(s)\right]$$
$$- z_{o_{pv}}(s) \cdot I_{o_{pv}}(s). \quad (29)$$

Eq. (29) implies the closed-loop control of the PV converter, where the dynamics influenced by MPPT are characterized by $V_{C_{pv}}^*$, input voltage $V_{C_{pv}}$, and output current $I_{o_{pv}}$. The output voltage includes two main components. The first one is the controlled voltage source determined by the reference $V_{C_{pv}}^*$, and the measured value of the input voltage of the converter $V_{C_{pv}}$. The second one is the output impedance z_{opv}. Fig. 7 shows the equivalent model of the closed-loop control of HPS system considering the PV converter dynamic.

$$I_{out}(s) = \frac{(R_L + z_{th}(s))\left(H(s)V_{ref} + (z_{sc_{oc}}(s) + z_{soc}(s)))I_{opv}(s)\right) - (R_L V_{th}(s))}{z_{out}(s)(R_L + z_{th}(s)) + R_L z_{th}(s)}. \tag{14}$$
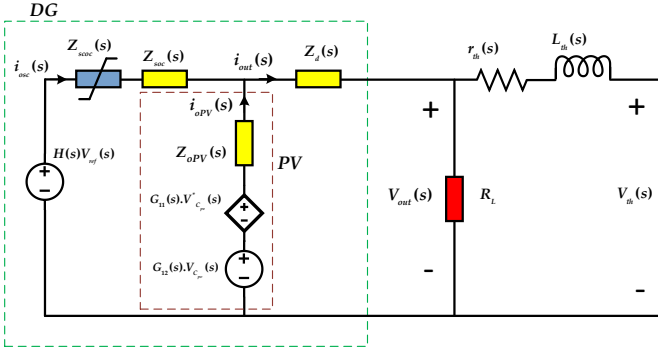

Fig. 7: Equivalent small signal model of HPS

Fig. 8: Dominant frequency of DG1 unit for varying line resistances.

Now, by substituting $I_{o_{pv}}(s)$ (obtained from (29)) in (10), substituting $I_{o_{sc}(s)}$ in (9), and also substituting $V_{out}(s)$ in (13), the characteristic equation of the closed-loop system considering the PV converter dynamics is obtained as follows

$$\left(z_{o_{pv}}(s) + z_{scoc}(s) + z_{soc}(s)\right) \cdot z_l(s)R_L + \left(R_L + z_l(s)\right)$$
$$\times \left(z_{scoc}(s) + z_{soc}(s) + z_d(s)\right)z_{o_{pv}(s)} = 0 \tag{30}$$

The impact of the PV converter dynamics on the stability of the overall DC-MG will be studied in section IV-B.

IV. STABILITY ANALYSIS OF CLOSED-LOOP SYSTEM

A. Effect of DG System Parameters

The roots of the characteristic equation are affected by the system's parameters, including current droop, line impedance, load, SOC controller, and the output impedance of the system. Hence, an eigenvalue analysis is performed to investigate the dynamic performance under varying parameters. To examine the effect of line impedance, it is assumed that DG1 supplies a local load of 2 kW and is connected to the grid through a distribution line. Also, it is assumed that SC is in the discharge operation mode. It is worth mentioning that the analysis is conducted for the case where there is no virtual impedance loop and only droop control is used. At first, to study the effect of line resistance, it is assumed that the impedance line is fully-resistive (.i.e $l_{line} = 0$). The dominant low-frequency modes of the DG1 are calculated for varying line resistances from zero to 46.1 $m\Omega$, as shown in Fig. 8.

As seen, the dominant low-frequency modes of the DG unit are between 15-25 Hz, and as the line resistance increases, the damping ratio is increased. Also, as it can be observed, the system will be unstable for the line resistance values smaller than 9.2 $m\Omega$ ($r_{line} < 9.2$ $m\Omega$). Nevertheless, enlarging the line resistance is not a practical and feasible solution as it increases the losses and corrupts the voltage profile. Furthermore, it has a negative effect on the current-sharing accuracy. To analyze the effect of line inductance on the stability performance of the DC-MG, it is supposed that the line resistance is adjusted at
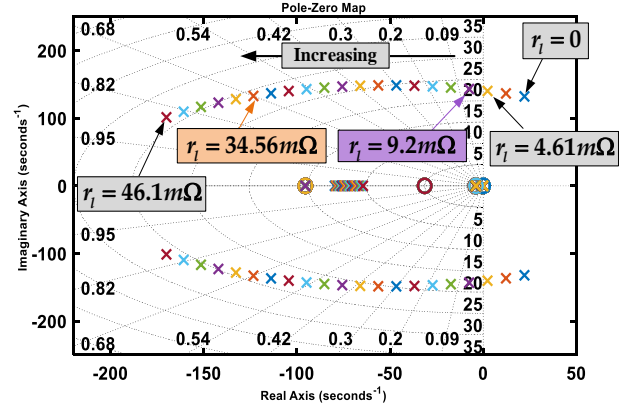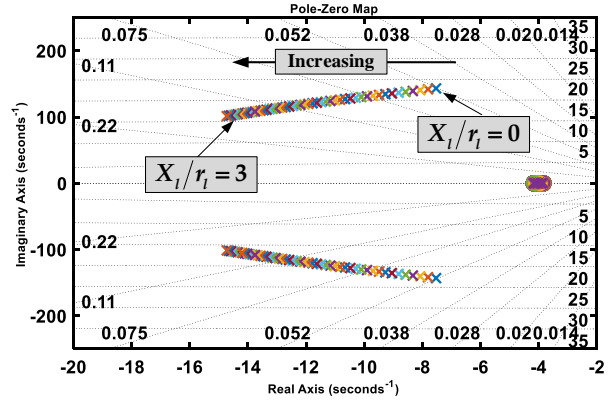

Fig. 9: Dominant low-frequency modes of DG1 when XL_l/R_l ratio changes from 0 to 0.2.

the worst operation condition (.i.e, $r_{line} = 9.2$ $m\Omega$), and the dominant low-frequency modes are calculated when the line inductance varies from 0 to 0.11 mH. The variation of the dominant low-frequency modes of DG1 are shown in Fig. 9. As depicted, the system performs better with an increased line inductance. The parameters of the SOC controller, on the other hand, can influence the system damping ratio. Accordingly, an small-signal analysis is conducted for DG unit to study the impact of the proportional gain (k_p), and integral gain (k_i) of the voltage controller (G_{soc}) on the operation of the DC-MG. It is assumed that the parameters of line impedance are set as ($r_{line} = 6.9$ $m\Omega$) and ($l_{line} = 4.4$ μH) and the local load is ($R_{load} = 2$ kW). Also, the droop coefficient is set on a specified value ($R_d = 0.057$) where the maximum voltage drop will not exceed the permissible allowable value. The results are shown in Fig. 10 and Fig. 11. As observed, the dominant low-frequency modes are more impacted by the proportional gain than the integral gain.

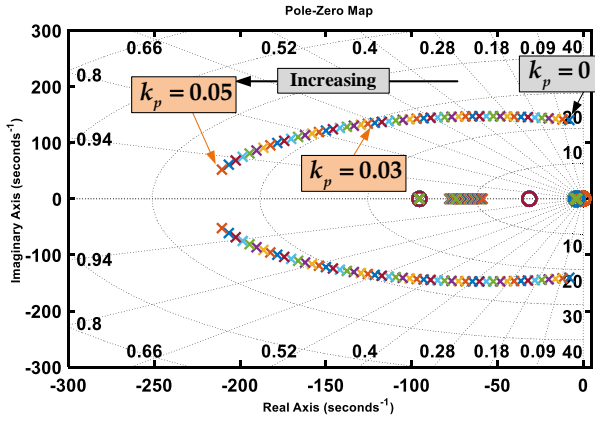Next, the virtual impedance loop is included in the voltage

8

Fig. 10: Dominant low-frequency modes of DG1 when k_p changes from 0 to 0.05.
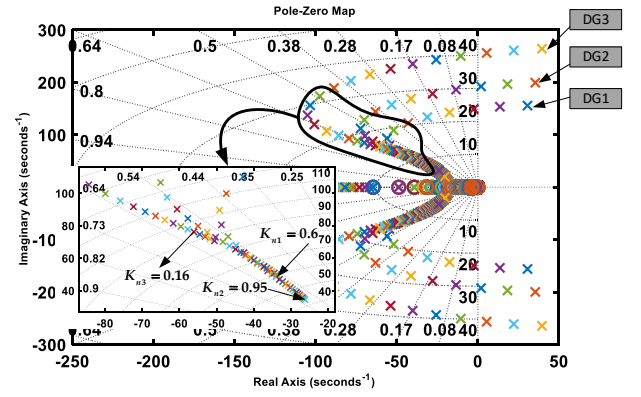

Fig. 12: Dominant low-frequency modes of DG1 when K_n of virtual impedance loop changes from -0.3 to 1.
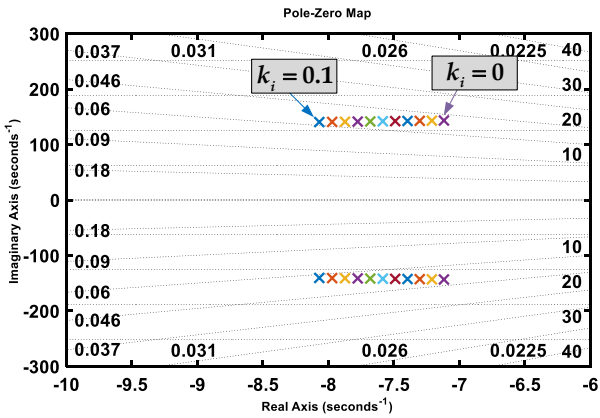

Fig. 11: Dominant low-frequency modes of DG1 when k_i changes from 0 to 0.1.

coefficient has a small impact on the frequency oscillations, and the characteristic equation of the closed-loop system has two complex conjugate poles with a small damping ratio.
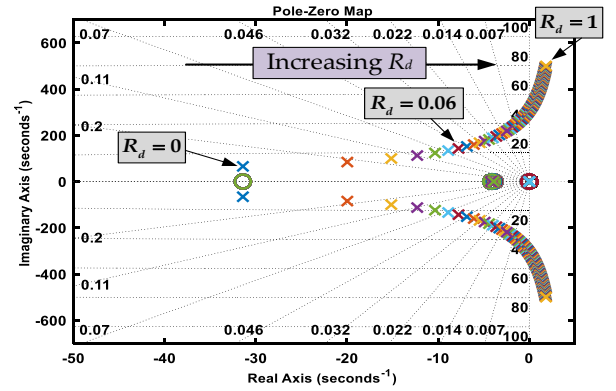

Fig. 13: Dominant low-frequency modes when R_d varies from 0 to 1.

control loop to damp the low-frequency modes of the DC-MG. The dominant low-frequency modes are calculated for DG_1, DG_2, and DG_3 when the values of K_n vary from -0.3 to 2. The eigenvalues movement for different values of K_n is shown in Fig. 12. The line resistance and line inductance are considered to be 9.2 $m\Omega$ and 4.4 μH, respectively, to provide the worst-case operational condition. Furthermore, it is assumed that SC is in the discharge operation mode.

The droop coefficients are adjusted to 0.057, 0.114, and 0.228, respectively. As it can be seen, the DGs stability is deteriorated for the negative values of K_n and it is enhanced with an increased K_n. Thus, in order to achieve a favorable damping ratio ($DF = 0.7$), K_{n1}, K_{n2}, and K_{n3} are chosen equal to 0.6, 0.9, and 0.16, respectively.

Moreover, an eigenvalue analysis is performed to investigate the effect of droop coefficient R_d on the stability performance. It is assumed that droop coefficient Fig. 13 shows the dominant low-frequency modes when R_d varies from 0 to 1. To analyze the effect of R_d on the stability performance of the DC-MG, it is supposed that the line resistance and line inductance are set to be 9.2 $m\Omega$ and 4.4 mH, respectively, to provide the worst-case operational condition. Also, DG supplies a local load of 2 kW. It can be observed from Fig. 13 that the droop

B. Analysis of Small-signal Stability of the Overall DC-MG

As shown in Fig. 14, an equivalent model is provided to investigate the small-signal stability of the overall DC-MG in Fig. 1. As observed, each voltage-controlled converter is modeled by an independent voltage source in series with the closed-loop impedance of the SC converter. Small-signal analysis is then carried out to evaluate the impact of the proposed control loop on the system's dynamic performance. For this aim, the linear models of loads, lines, and all DG units are obtained in the Laplace domain. The dominant low-frequency modes of the overall DC-MG are determined using the characteristic equation, which is expressed using impedance analysis. The mesh impedance matrix can be calculated as

$$\mathbf{Z_{MG}(s)} = \begin{bmatrix} Z_{MG11}(s) & Z_{MG12}(s) & Z_{MG13}(s) \\ Z_{MG21}(s) & Z_{MG22}(s) & Z_{MG23}(s) \\ Z_{MG31}(s) & Z_{MG32}(s) & Z_{MG33}(s) \end{bmatrix} \quad (31)$$
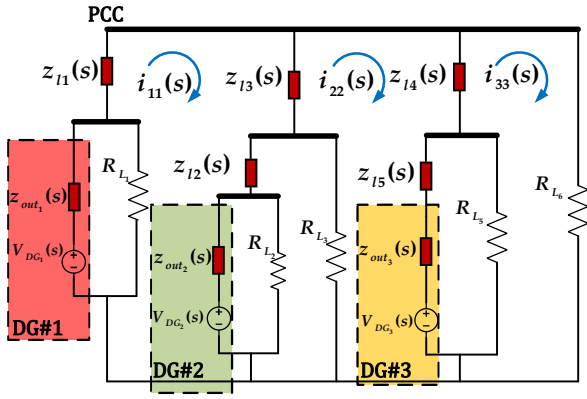
Fig. 14: Equivalent model of overall DC-MG (DG4 is in standby mode)
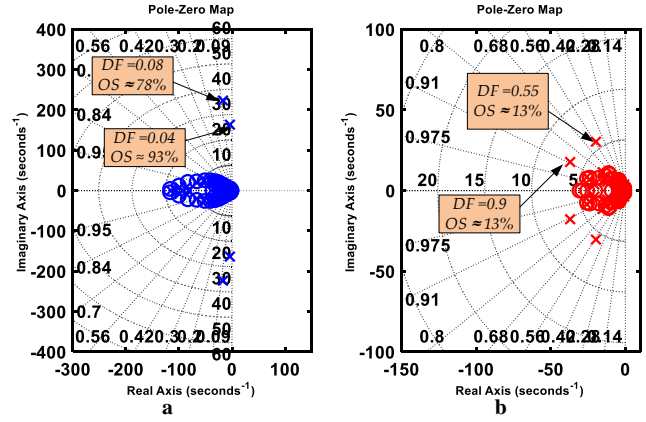
.

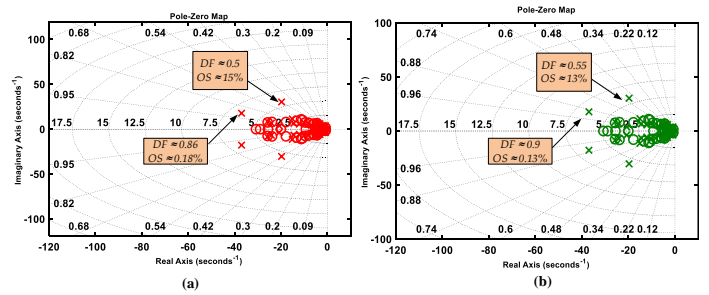Fig. 15: Dominant low-frequency modes of overall DC-MG: (a) without proposed control, (b) with proposed control.

Fig. 16: Dominant low-frequency modes of overall DC-MG: (a) without considering PV converter dynamic, (b) with considering PV converter dynamic

where

$$
\begin{aligned}
Z_{\mathrm{MG}11}(s) &= [Z_{\mathrm{out}1}(s) \parallel R_{\mathrm{L}1} + ((Z_{\mathrm{out}2}(s) \parallel R_{\mathrm{L}2}) \\
&\quad + Z_{L2}(s)) \parallel R_{\mathrm{L}3} + Z_{L1}(s) + Z_{L3}(s)] \\
Z_{\mathrm{MG}12}(s) &= Z_{\mathrm{MG}21}(s) = -[(Z_{\mathrm{out}2}(s) \parallel R_{\mathrm{L}2} \\
&\quad + Z_{L2}(s)) \parallel R_{\mathrm{L}3} + Z_{L3}(s)] \\
Z_{\mathrm{MG}13}(s) &= Z_{\mathrm{MG}31}(s) = 0 \\
Z_{\mathrm{MG}22}(s) &= [(Z_{\mathrm{out}2}(s) \parallel R_{\mathrm{L}2} + Z_{L2}(s)) \parallel R_{\mathrm{L}3} \\
&\quad + (Z_{\mathrm{out}3}(s) + Z_{L5}(s)) \parallel R_{\mathrm{L}5} \\
&\quad + Z_{L3}(s) + Z_{L4}(s)] \\
Z_{\mathrm{MG}23}(s) &= Z_{\mathrm{MG}32}(s) = -[(Z_{\mathrm{out}2}(s) + Z_{L5}(s)) \parallel R_{\mathrm{L}5} \\
&\quad + Z_{L4}(s)] \\
Z_{\mathrm{MG}33}(s) &= (Z_{\mathrm{out}3}(s) + Z_{L5}(s)) \parallel R_{\mathrm{L}5} \\
&\quad + Z_{L4}(s) + R_{\mathrm{L}6}.
\end{aligned}
\tag{32}
$$

where

$$
\begin{aligned}
Z_{\mathrm{out}1}(s) &= z_{\mathrm{scoc}1}(s) + z_{\mathrm{soc}1}(s) + z_{\mathrm{d}1}(s) \\
Z_{\mathrm{out}2}(s) &= z_{\mathrm{scoc}2}(s) + z_{\mathrm{d}2}(s) \\
Z_{\mathrm{out}3}(s) &= z_{\mathrm{scoc}3}(s) + z_{\mathrm{d}3}(s).
\end{aligned}
\tag{33}
$$

The dominant low-frequency modes of the DC-MG with and without the proposed control loop are shown in Fig.15. As the figure illustrates, the proposed control loop provides the system with a higher damping ratio than the conventional control (without the proposed control loop). In addition, the low-frequency modes of the system in two cases (a) without considering PV converter dynamic and (b) with considering PV converter dynamic are obtained and shown in Fig. 16. As can be seen, the results with and without considering the PV converter dynamics are in close agreement with each other. It implies that the PV converter dynamic does not affect much the frequency modes of overall DC-MG obtained by neglecting the PV converter dynamics.

V. TUNING OF REGULATION COEFFICIENT USING INN-BASED APPROACH

The performance of virtual resistive impedance loop is highly influenced by the regulation coefficient K_n, which should be adjusted optimally. The selection of optimal coefficient based on random trial-and-error method and eigen-participation analysis is a very time-consuming process, which requires many selections and many computer simulations. Besides, once the operating point changes highly, ensuring a favorable response is a challenging task. The intelligent methods rehabilitate such deficiencies in acquiring a robust performance in different operating conditions of microgrids [29]. The INN as a powerful tool is a suitable option to achieve the proposed control objectives. The schematic diagram of the proposed INN-based regulation scheme is depicted in Fig. 17. Input signals of the INN-based regulation unit contain the MG output and a set of basic data. The intelligent unit provides an accurate online adaptation of the regulation coefficient K_n embedded in the virtual impedance loop and thereby enhances the stability of the converter control system. This adaptive feature improves the converter's robustness against different uncertainties and a wide range of operating states. The proposed method is detailed in Fig. 18. The INN output is a supplementary regulation coefficient K_{1n} to update the constant regulation coefficient K_{2n}. The key functionality of the proposed structure is to minimize the voltage variation. Therefore, appropriate set points are created by INN and applied to the output of the inner loop to achieve a stable control operation.

The processing units in an INN, which are inherently non-linear, are known as neurons. Each neuron contains three
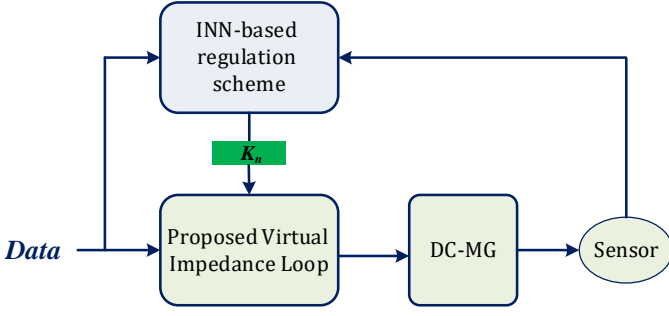
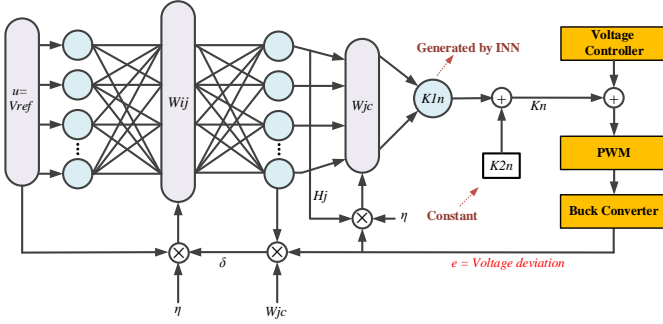Fig. 17: The general schematic for online tuning of regulation coefficient

Fig. 18: Structure of the proposed INN-based regulation scheme.

basic elements including weights $w_{ij} = [w_{1j}, w_{2j}, ..., w_{nj}]$, an activation function $f(net)$, and a bias parameter φ [30]. Various functions such as sign, tangent sigmoid, and logarithmic sigmoid can be used for the activation function $g(net)$. The output of the hidden layer is calculated based on the weighted input and bias as mathematically shown in (34):

$$H_j = g\left(\sum_{i=1}^{n} w_{ij}u_i + \varphi\right) \qquad j = 1, 2, ..., L \qquad (34)$$

where L is the number of nodes in the hidden layer; and u_i is the input signals.

Then, the output of the output layer can be obtained as follows:

$$O_c = \sum_{j=1}^{L} H_j w_{jc} + \varphi \qquad c = 1, 2, ..., m \qquad (35)$$

where m is the number of nodes in the output layer; and H_j is the output of the hidden layer.

The learning procedure deals with the minimization of mean squared error as follows:

$$E = \frac{1}{2}\sum_{r=1}^{N} e_r^2 \qquad (36)$$

where $e = V_{out} - V_{ref}$.

The weights of the INN are updated based on supervised feedback approach in which back-propagation algorithm is used for the learning procedure [31]. Back propagation is a very well-known algorithm that is available in standard software like MATLAB. Therefore, it will not be described further here.

The calculated error value in (36) is employed to update the INN weights as follows:

$$w_{ij}(k+1) = w_{ij}(k) + \Delta w_{ij} = w_{ij}(k) + \eta \delta u$$
$$i = 1, 2, ..., n \qquad j = 1, 2, ..., L \qquad (37)$$

$$w_{jc}(k+1) = w_{jc}(k) + \Delta w_{jc} = w_{jc}(k) + \eta H_j e$$
$$j = 1, 2, ..., L \qquad c = 1, 2, ..., m \qquad (38)$$

where, Δw_{ij} and Δw_{jc} are calculated based on Eqs. (39)-(40). All parameters used to calculate of Δw_{ij} and Δw_{jc} can be observed in Fig. 18.

$$\Delta w_{jc} = -\eta \frac{\partial E}{\partial w_{jc}}, \quad \frac{\partial E}{\partial w_{jc}} = \frac{\partial E}{\partial y}\frac{\partial y}{\partial x}\frac{\partial x}{\partial net_c}\frac{\partial net_c}{\partial w_{jc}},$$
$$\frac{\partial net_c}{\partial w_{jc}} = f'(net_c)$$
$$\frac{\partial net_c}{\partial w_{jc}} = H_j, \quad \frac{\partial E}{\partial y}\frac{\partial y}{\partial X}\frac{\partial X}{\partial net_c} = e, \quad \Delta w_{jc} = \eta H_j e \quad (39)$$

$$\Delta w_{ij} = -\eta \frac{\partial E}{\partial w_{ij}}, \quad \frac{\partial E}{\partial w_{ij}} = \frac{\partial E}{\partial y}\frac{\partial y}{\partial x}\frac{\partial x}{\partial net_c}\frac{\partial net_c}{\partial H_j}\frac{\partial H_j}{\partial net_j}\frac{\partial net_j}{\partial w_{ij}}$$
$$\frac{\partial x}{\partial net_c} = f'(net_c), \quad \frac{\partial net_c}{\partial H_j} = w_{jc},$$
$$\frac{\partial H_j}{\partial net_j} = f'(net_j), \quad \frac{\partial net_j}{\partial w_{jc}} = u$$
$$\Delta w_{ij} = \eta \delta f'(net_c) w_{jc} f'(net_j) u = \eta \delta u \quad (40)$$

It is to be noted that in the Fig. 18, W_1 represents the weight vector for the hidden layer whereas W_2 is similarly deployed for the output; and η is the learning rate.

The considered INN is trained by the response for a set of different scenarios and based on the system dynamics to online prepare the virtual impedance coefficient (K_n). In the design process of the proposed INN based fine-tuning structure, it is considered that the input layer of INN has twenty linear neurons, and there are ten nonlinear neurons for the hidden layer. The number of neurons in input/hidden layers is determined through a trial and error process. Besides, INN's output layer must contain an analogous number of neurons to the control variables. Since the control variables include only one regulation coefficient, one linear neuron is thus considered in the output layer.

VI. SIMULATION RESULTS

Various case studies are conducted to assess the performance of the proposed control scheme. The DC-MG shown in Fig. 1 is simulated in MATLAB/Simulink software environment. The simulations are carried out on a MATLAB/Simulink environment on a laptop with a core i7-4510U CPU @ 2.6GHz, RAM 6GB. The dynamic performance is examined by applying a sequence of step load changes at PCC for Bus4 as shown in Fig. 19. As the figure indicates, a load increase of 0.75 kW at t = 1s is assumed, followed by a load decrease of 0.75 kW at t = 3s, a load increase of 1.1 kW at t = 4s, and a load increase of 1.9 kW at t = 6s. The deviations in output currents of DG1, ESS1, and ESS2 are shown in Fig. 20. As the results imply, with traditional droop control, the output currents of

DG1, ESS1, and ESS2 oscillate with frequencies of 25.7 Hz, 22.2 Hz, and 41 Hz, respectively. The figure also indicates that, by using the proposed adaptive virtual impedance loop, significant reductions in the oscillations of output currents are achieved. The generated regulation coefficients by INN-based approach under the applied load changes are presented in Fig. 21. The figure reveals that the INN-based approach regulates the virtual impedance loop such that the fluctuations in the output currents are highly attenuated. The following conditions are considered to update k_n during case studies: 1- The error $(V_{ref}\text{-}V_{out}) \leq 0.05$. 2- The damping ratio not be less than 0.6. It is be noted that a logarithmic decrement method is used to calculate the damping ratio. In the simulation model for both offline simulation and HiL tests, the logarithmic decrement method is implemented by using an embedded Matlab Function block.

To study the impact of K_n on the current-sharing accuracy, it is assumed that the loading is changed under sequence steps, as in scenario 1. Figs. 22−24 show the error of current sharing for DG$_1$, ESS$_1$ and ESS$_2$, respectively. It can be seen that using the proposed control strategy brings the error close to zero, while without the proposed control strategy, the error remains in the interval [-2,2]. To further confirm the effectiveness of the proposed method, a comparison has been conducted between the proposed method and a prior work reported on low-frequency oscillation damping [25]. Fig. 25 and 26 show the comparison results, the dynamic response of output current of DG1, ESS1, and ESS2 is shown in Fig. 25, the current-sharing error of DG1, ESS1, and ESS2 is shown in Fig. 26. As it can be seen, both methods are characterized by good dynamic properties. From a point-view of current-sharing accuracy, the proposed method has clear superiority compared to the method reported in [25]. A study is carried out to assess the robustness of the proposed control scheme against the variation of the parameters of impedance lines. In this study, it is assumed that the load at Bus4 is increased. The output current of DG$_1$ unit in the cases of high and low impedance lines utilizing the droop control is shown in Fig.27. As observed, while the system is stable for the high impedance lines, it becomes unstable for low impedance lines. In contrast, the output current of the DG$_1$ unit using the proposed control is shown in Fig.28. As can be seen, the proposed control method offers superior robustness performance against the low impedance lines compared to the droop control.

A stability analysis is also performed to further clarify the robustness properties of the proposed control scheme. Accordingly, the dominant low-frequency modes of the overall DC-MG are calculated in the cases of low and high impedance lines for the droop control method and in the case of low impedance lines for the proposed control strategy. The results are depicted in Fig.29. As can be seen, when the droop control is used, the eigenvalues are in the right-half plane with a negative damping ratio equal to -0.066 for lines with lower impedances. In this case, the system experiences an instability mode. While for high impedance lines, the damping ratio is 0.55, and the system stability properties are suitable. In contrast, when the proposed control scheme is applied, the dominant low-frequency modes suggest that the system has good stability properties in the case
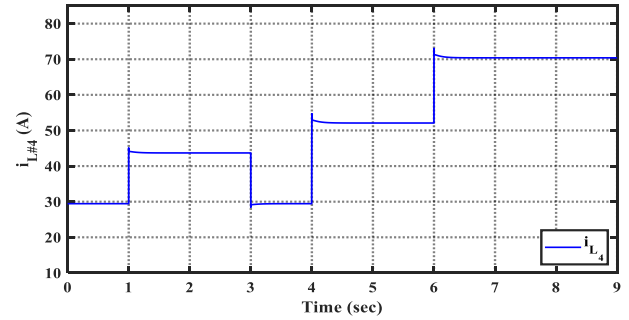

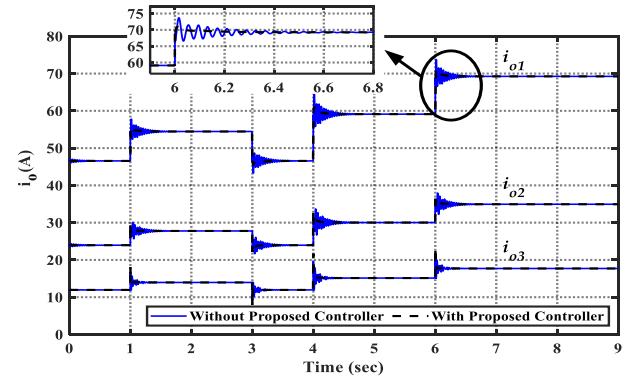Fig. 19: Variations in Load at Bus4.

Fig. 20: Output currents of DG1, ESS1, and ESS2 when Load$_4$ varies in a programmed sequence.
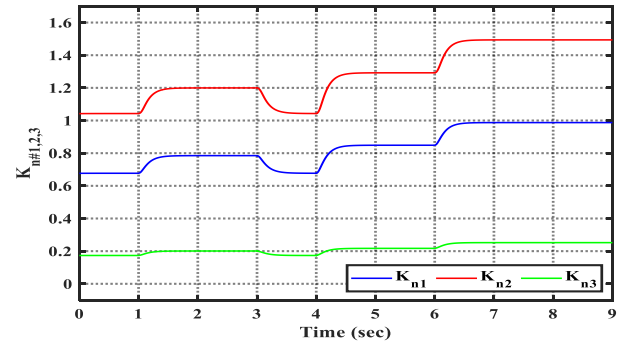

Fig. 21: Variations of K_n coefficient under the changes in operation conditions.

of low impedance lines with a damping ratio equal to 0.63. This ensures the robust performance of the proposed control scheme against the parameter changes.

Moreover, to investigate the performance of the INN-based approach to deal with critical conditions in DC-MG operation, K_c gain in the voltage control loop is set at 1.0 such that the inner loop stability of DG unit is adversely affected. The dominant low-frequency modes of the overall DC-MG are shown in Fig.30. In the figure, the blue poles-zeros represent the offline approach and the red ones correspond the proposed INN-based approach. In the offline approach, the regulation coefficients associated with virtual impedance loop are the same obtained in section IV-A. As observed, the system falls into an instability region without the INN-based approach. In contrast, the feature of the proposed INN results in a stable operation of
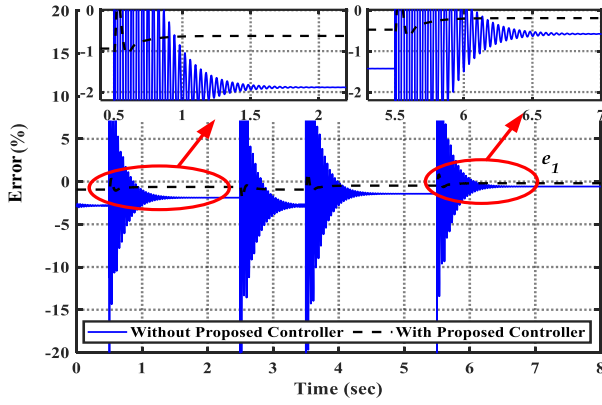
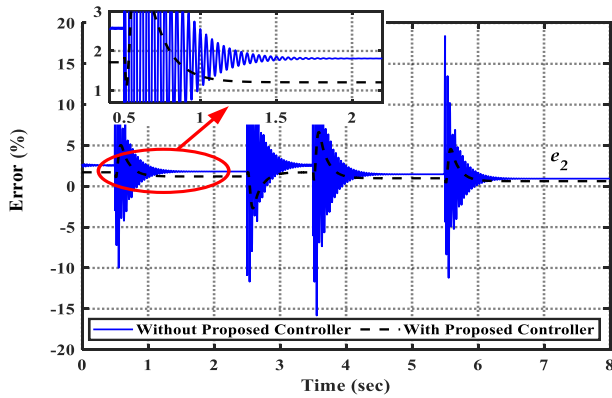Fig. 22: Current-sharing error of DG1 under for loading changes

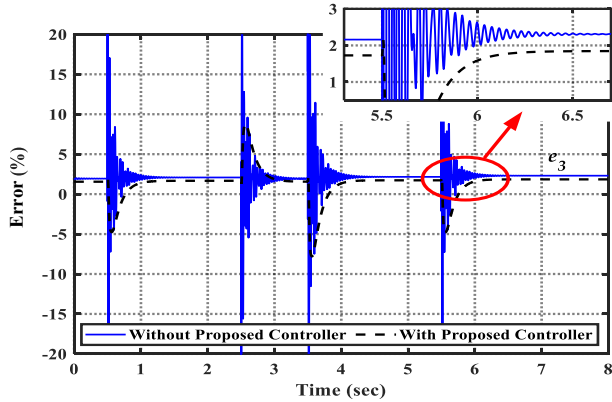Fig. 23: Current-sharing error of ESS1 under for loading changes

Fig. 24: Current-sharing error of ESS2 under for loading changes
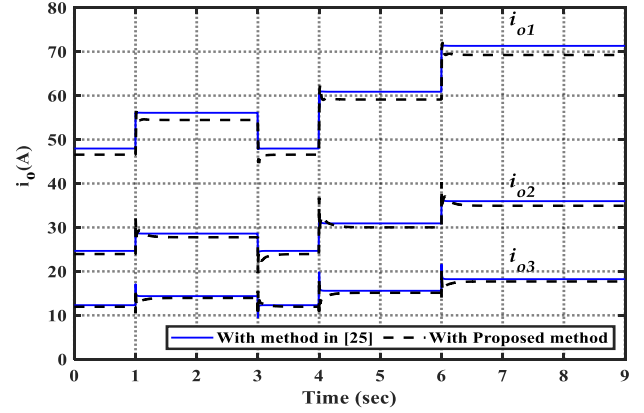

Fig. 25: Output currents of DG1, ESS1, and ESS2 when load#4 varies in a programmed sequence.
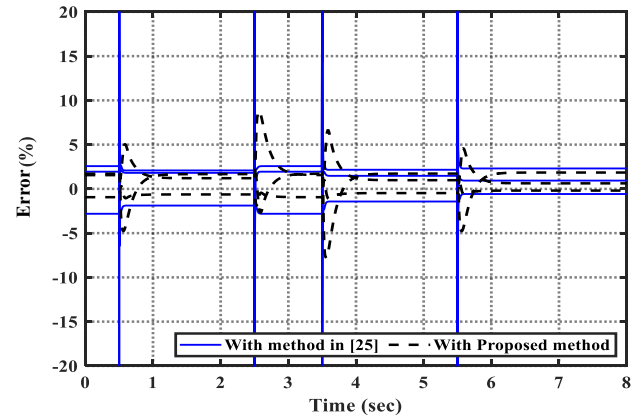

Fig. 26: Current-sharing error of DG1, ESS1, and ESS2 when load#4 varies in a programmed sequence.
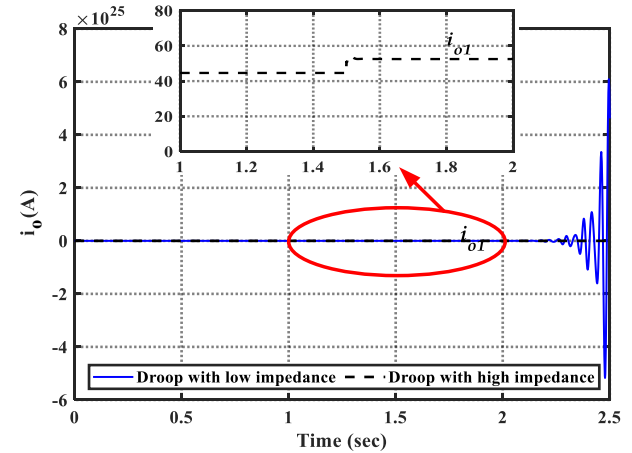

Fig. 27: Output current of DG_1 with droop control in the cases low and high impedance lines

the DC-MG and makes the proposed virtual impedance loop an online controller to support a wider range of operating points. Fig. 31 shows the output currents of the DG1, ESS1, and ESS2 with the proposed INN-based virtual impedance loop.

VII. HARDWARE IN THE LOOP VALIDATION

The HIL simulation platform is built based on the real-time simulator, OPAL-RT-OP5600, and dSPACE MicroLabBox. Fig. 32 shows a detailed structure of the HIL system used to verify

the proposed control scheme. The system plant, which is the DC-MG without its controllers, is modeled in OP5600. The control loops, including voltage control, droop control, charge regulator control, and virtual impedance loop, which determine the control commands at 20 kHz switching rate for the convert-ers, are modeled in the dSPACE MicroLabBox (DS1202). The
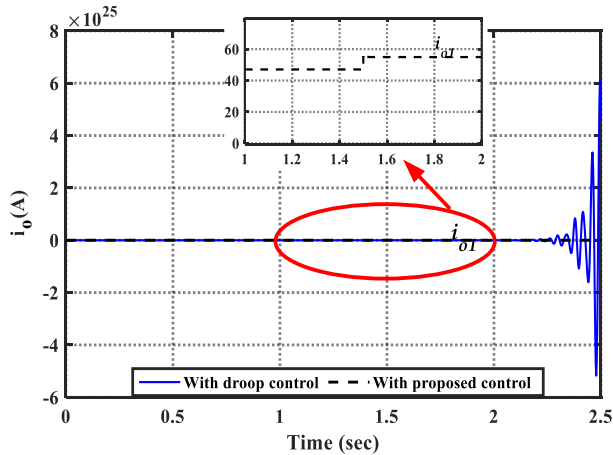
Fig. 28: Output current of DG$_1$ with proposed control and droop control in the case of low impedance lines
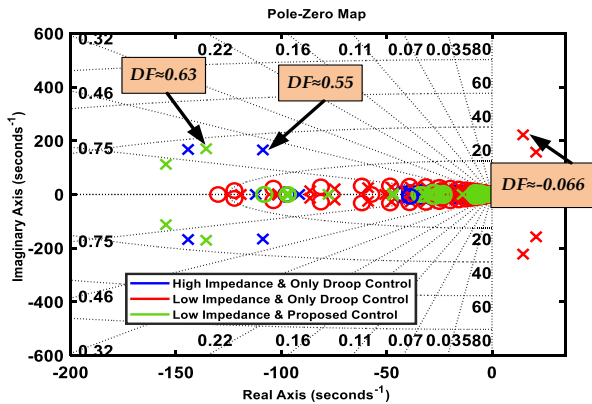

Fig. 29: Dominant low-frequency modes of overall DC-MG with droop control for both low- and high-impedance lines (red-blue) and with proposed control for low-impedance lines (green)
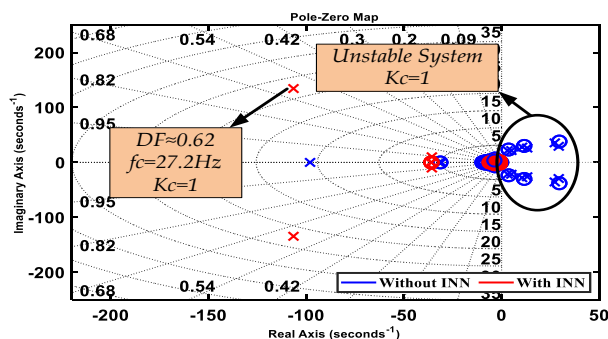

Fig. 30: Dominant low-frequency modes of the overall DC-MG with and without INN-based approach in case of $K_c = 1$.

DS1202 generates the PWM switching signals for the system executed in OPAL-RT. The dSPACE MicroLabBox controller provides an example of rapid control prototyping where the focus is the development and verification of different control methods rather than the implementation in a DSP requiring programming in C.

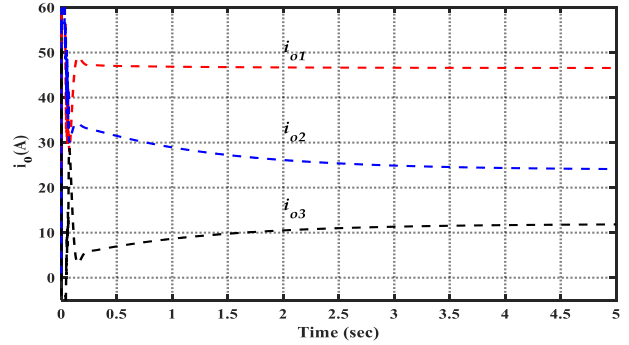In the presented HIL setup, Control Desk and RT-Lab are the

Fig. 31: Output currents of DG1, ESS1, and ESS2 with INN-based virtual impedance loop in case of $K_c = 1$.

simulation platforms for dSPACE and OPAL-RT, respectively. Both OP5600 and DS1202 are connected to a Windows-based host computer using a TCP/IP connection. Moreover, to ensure the accuracy of the comparison, the parameters of the controller used in the HIL experiment are consistent with those in the previous simulation. The analog output channels of OP5600 have been used to send the simulated plant's measured voltage and current signals to the analog input channels of DS1202. The analog output channels of DS1202 have been used to send control signals to the analog input channels of OPAL-RT. It should be noted that all the signals are normalized as the maximum limit on the I/O signals is ± 16 V for OPARL-RT and ± 10 V for dSPACE. The detailed structure of the HIL system used to validate the proposed control scheme is depicted in Fig. 32. The computation time should be scaled over the sampling time used. Also, for the HIL setup, the sampling times for both OPAL-RT and DS1202 systems were 10 μs.

A real-time scenario is made to evaluate the proposed control strategy's dynamic performance under the DG units' plug-and-play operation. For this goal, it is assumed that DG4 with a rated power of 1 kW, suppling a local load of 0.5 kW, is connected to Bus5 through the distribution line z_{l_7} ($z_{l_7}=z_{l_1}$) at $t = 1$s, and then, DG4 is disconnected from the MG at $t = 4$s. While the output currents of DG1 and DG4 are displayed in Fig. 22, those of ESS1 and ESS2 are shown in Fig. 34. Without the proposed control method, undesired oscillations in the output currents appear. Whereas, by the use of the proposed virtual impedance loop, the low-frequency oscillations are omitted entirely. Another real-time scenario for the proposed control scheme evaluation is investigated, which involves a dynamic change in a nonlinear load. It is assumed that a constant-power load (CPL) with a rated power of 0.5 kW is connected to Bus#4 through a line with an impedance equal to z_{l_6}. The CPL is modeled by a dc/dc buck converter operated in the voltage-control mode supplying a resistive load. The results are shown in Fig. 35. A comparison between the output currents of the DG1, ESS1, and ESS2 obtained for the traditional and proposed control strategies shows that the proposed intelligent virtual impedance loop remarkably diminishes the current's low-frequency oscillations during transient conditions.

VIII. CONCLUSION

This paper proposes an active control method to enhance the dynamic performance of a droop-controlled DC-MG. The
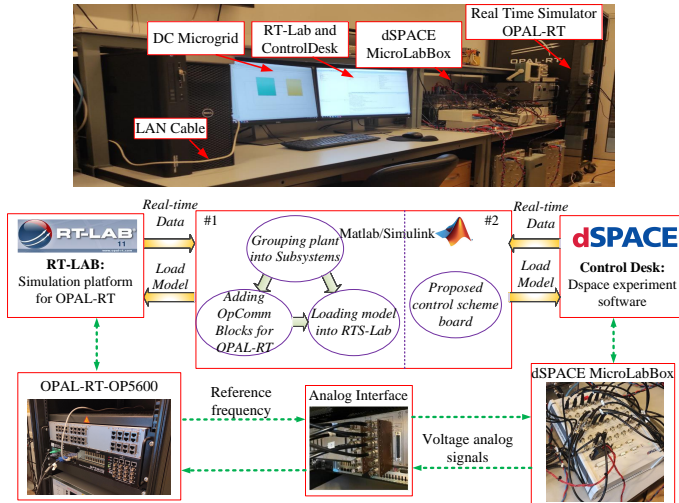
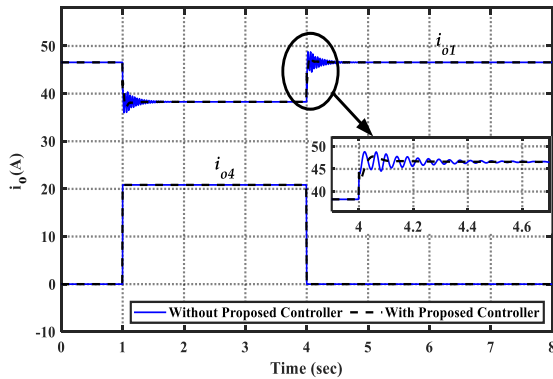Fig. 32: HIL experimental setup to validate the proposed control scheme

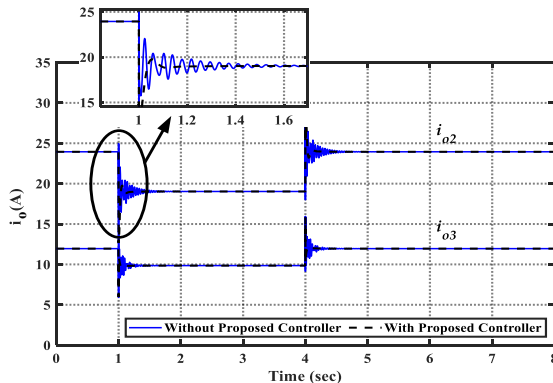Fig. 33: Output currents of DG1,4 when DG4 connects to Bus5 and then disconnects.

Fig. 34: Output currents of ESS1,2 when DG4 connects to Bus5 and then disconnects.

proposed approach relies on augmenting a virtual resistive impedance loop to the inner loop of the control system of the converters. The principle of the presented damping loop is based on regulating the output impedance of each converters without manipulating the voltage controller. The INN method was proposed to adjust the damping coefficient of the virtual impedance loop. The initial tuning of the damping coefficient
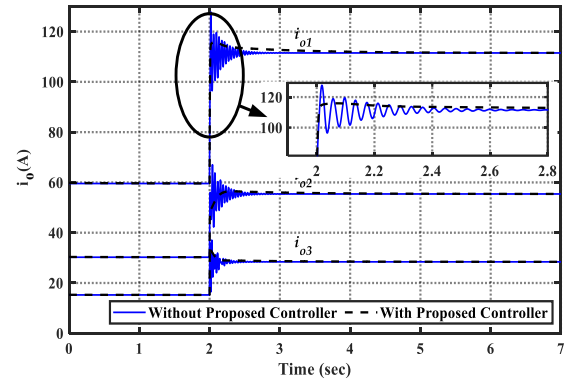

Fig. 35: Output currents of DG1, ESS1, and ESS2 when CPL increases from 1.5 kW to 3.5 kW.

was based on a small-signal stability analysis. The results confirmed that the proposed control scheme can: (i) reduce the low-frequency oscillations compared to the case without a damping loop; (ii) indicate a robust performance against the unknown parameters; (iii) deal with various sorts of loads; (iv) support a wider range of operating conditions. Finally, the proposed control scheme was verified by the HIL simulation platform.

REFERENCES

[1] A. Abhishek, A. Ranjan, S. Devassy, B. K. Verma, S. K. Ram, and A. K. Dhakar, "Review of hierarchical control strategies for dc microgrid," *IET Renewable Power Generation*, vol. 14, no. 10, pp. 1631–1640, 2020.

[2] Q. Xu, N. Vafamand, L. Chen, T. Dragičevi´c, L. Xie, and F. Blaabjerg, "Review on advanced control technologies for bidirectional DC/DC converters in DC microgrids," *IEEE J. Emerg. Sel. Topics Power Electron.*, vol. 9, no. 2, pp. 1205–1221, 2020.

[3] S. Liu, P. Su, and L. Zhang, "A virtual negative inductor stabilizing strategy for dc microgrid with constant power loads," *IEEE Access*, vol. 6, pp. 59728–59741, 2018.

[4] A. A. Derbas and M. Hamzeh, "A new power sharing method for improving power management in dc microgrid with power electronic interfaced distributed generations," in *2019 27th Iranian Conference on Electrical Engineering (ICEE)*. IEEE, 2019, pp. 624–629.

[5] M. Ahmed, L. Meegahapola, A. Vahidnia, and M. Datta, "Stability and control aspects of microgrid architectures–a comprehensive review," *IEEE Access*, vol. 8, pp. 144 730–144 766, 2020.

[6] F. S. Al-Ismail, "Dc microgrid planning, operation, and control: A comprehensive review," *IEEE Access*, vol. 9, pp. 36 154–36 172, 2021.

[7] Y. Liu, X. Zhuang, Q. Zhang, M. Arslan, and H. Guo, "A novel droop control method based on virtual frequency in dc microgrid," *International Journal of Electrical Power & Energy Systems*, vol. 119, p. 105946, 2020.

[8] X.-K. Liu, Y.-W. Wang, P. Lin, and P. Wang, "Distributed supervisory secondary control for a dc microgrid," *IEEE Transactions on Energy Conversion*, vol. 35, no. 4, pp. 1736–1746, 2020.

[9] M. Zhang, Q. Xu, C. Zhang, and F. Blaabjerg"Decentralized Co-ordination and Stabilization of Hybrid Energy Storage Systems in DC Microgrids," *IEEE transactions on Smart Grid*, 2022, DOI: 10.1109/TSG.2022.3143111.

[10] O. Andres-Martinez, A. Flores-Tlacuahuac, O. F. Ruiz-Martinez, and J. C. Mayo-Maldonado, "Nonlinear model predictive stabilization of DC-DC boost converters with constant power loads," *IEEE J. Emerg. Sel. Topics Power Electron.*, vol. 9, no. 1, pp. 822–830, 2021.

[11] M. N. Hussain, R. Mishra, and V. Agarwal, "A frequency-dependent virtual impedance for voltage-regulating converters feeding constant power loads in a DC microgrid," *IEEE Trans. Ind. Appl.*, vol. 54, no. 6, pp. 5630–5639, Nov./Dec. 2018.

[12] M. Su, Z. Liu, Y. Sun, H. Han, and X. Hou, "Stability analysis and stabilization methods of DC microgrid with multiple parallel-connected DC–DC converters loaded by CPLs," *IEEE Trans. Smart Grid*, vol. 9, no. 1, pp. 132–142, Jan. 2018.

[13] J. Siegers, S. Arrua, and E. Santi, "Stabilizing controller design for multibus MVdc distribution systems using a passivity-based stability criterion and positive feedforward control," *IEEE J. Emerg. Sel. Topics Power Electron.*, vol. 5, no. 1, pp. 14–27, Mar. 2017.

[14] D. Majstorovic, I. Celanovic, N. D. Teslic, N. Celanovic, and V. A. Katic, "Ultralow-latency hardware-in-the-loop platform for rapid validation of power electronics designs," *IEEE Trans. Ind. Electron.*, vol. 58, no. 10, pp. 4708–4716, Oct. 2011.

[15] M. Cespedes, L. Xing, and J. Sun, "Constant-power load system stabilization by passive damping," *IEEE Trans. Power Electron.*, vol. 26, no. 7, pp. 1832–1836, Jul. 2011.

[16] Y. Gui, R. Han, J. M. Guerrero, J. C. Vasquez, B. Wei, and W. Kim, "Large-signal stability improvement of dc-dc converters in dc microgrid," *IEEE Transactions on Energy Conversion*, vol. 36, no. 3, pp. 2534–2544, Sept. 2021.

[17] L. Zhou, W. Wu, Y. Chen, Z. He, X. Zhou, X. Huang, L. Yang, A. Luo, and J. M. Guerrero, "Virtual positive-damping reshaped impedance stability control method for the offshore mvdc system," *IEEE Transactions on Power Electronics*, vol. 34, no. 5, pp. 4951–4966, 2019.

[18] M. N. Hussain and V. Agarwal, "A novel feedforward stabilizing technique to damp power oscillations caused by DC-DC converters fed from a DC bus," *IEEE J. Emerg. Sel. Topics Power Electron.*, vol. 8, no. 2, pp. 1528–1528, June 2020.

[19] B. He, W. Chen, X. Li, L. Shu, and X. Ruan, "A power adaptive impedance reshaping strategy for cascaded DC system with buck-type constant power load," *IEEE Trans. Power Electron.*, early access, Feb. 8, 2022, doi: 10.1109/TPEL.2022.3149604.

[20] R. Kumar, R. Sharma, and A. Kumar, "Adaptive negative impedance strategy for stability improvement in dc microgrid with constant power loads," *Computers & Electrical Engineering*, vol. 94, p. 107296, 2021.

[21] M. Jami, Q. Shafiee, and H. Bevrani, "Dynamic improvement of dc microgrids using a dual approach based on virtual inertia," *Journal of Modern Power Systems and Clean Energy*, 2020.

[22] A. Hosseinipour and H. Hojabri, "Small-signal stability analysis and active damping control of dc microgrids integrated with distributed electric springs," *IEEE Transactions on Smart Grid*, vol. 11, no. 5, pp. 3737–3747, 2020.

[23] N. Rashidirad, M. Hamzeh, K. Sheshyekani, and E. Afjei, "High-frequency oscillations and their leading causes in dc microgrids," *IEEE Transactions on Energy Conversion*, vol. 32, no. 4, pp. 1479–1491, 2017.

[24] N. Rashidirad, M. Hamzeh, K. Sheshyekani, and E. Afjei, "An effective method for low-frequency oscillations damping in multibus dc microgrids," *IEEE Journal on Emerging and Selected Topics in Circuits and Systems*, vol. 7, no. 3, pp. 403–412, 2017.

[25] M. Hamzeh, M. Ghafouri, H. Karimi, K. Sheshyekani, and J. M. Guerrero, "Power oscillations damping in dc microgrids," *IEEE Transactions on Energy Conversion*, vol. 31, no. 3, pp. 970–980, 2016.

[26] A. -A. Derbas, M. Kheradmandi, M. Hamzeh and N. D. Hatziargyriou, "A Hybrid Power Sharing Control to Enhance the Small Signal Stability in DC Microgrids," in *IEEE Transactions on Smart Grid*, doi: 10.1109/TSG.2022.3156850

[27] J. Guo, T. Chen, B. Chaudhuri, and S. Y. R. Hui, "Stability of isolated microgrids with renewable generation and smart loads," *IEEE Transactions on Sustainable Energy*, vol. 11, no. 4, pp. 2845–2854, 2020.

[28] O. Lorzadeh, I. Lorzadeh, M. N. Soltani, and A. Hajizadeh, "Source side virtual RC damper-based stabilization technique for cascaded systems in DC microgrids," *IEEE Trans. Energy Convers.*, vol. 36, no. 3, pp. 1883–1895, Sep. 2021.

[29] A. -A. Derbas, A. Oshnoei, M. Kheradmandi, and F. Blaabjerg, "Intelligent Primary Control of Voltage Source Converters in AC Microgrids," *IECON 2022 - 48th Annual Conference of the IEEE Industrial Electronics Society*, pp. 1–6, 2022.

[30] R. Khezri, A. Oshnoei, A. Yazdani, and A. Mahmoudi, "Intelligent coordinators for automatic voltage regulator and power system stabiliser in a multi-machine power system," *IET Generation, Transmission & Distribution*, vol. 14, no. 23, pp. 5480–5490, 2020.

[31] H. Sorouri, M. Sedighizadeh, A. Oshnoei, and R. Khezri, "An intelligent adaptive control of dc–dc power buck converters," *International Journal of Electrical Power & Energy Systems*, vol. 141, p. 108099, 2022.